Aseismic transient slip on the Gofar transform fault, East Pacific Rise

Yajing Liu[a,b,1], Jeffrey J. McGuire[b,c], and Mark D. Behn[b,d]

[a]Department of Earth and Planetary Sciences, McGill University, Montréal, QC, Canada H3A 0E8; [b]Department of Geology and Geophysics, Woods Hole Oceanographic Institution, Woods Hole, MA 02543; [c]Earthquake Science Center, US Geological Survey, Moffett Field, CA 94035; and [d]Department of Earth and Environmental Sciences, Boston College, Chestnut Hill, MA 02467

Edited by Goran Ekstrom, Lamont-Doherty Earth Observatory of Columbia University, Palisades, NY, and approved March 19, 2020 (received for review August 6, 2019)

Oceanic transform faults display a unique combination of seismic and aseismic slip behavior, including a large globally averaged seismic deficit, and the local occurrence of repeating magnitude (M) ∼ 6 earthquakes with abundant foreshocks and seismic swarms, as on the Gofar transform of the East Pacific Rise and the Blanco Ridge in the northeast Pacific Ocean. However, the underlying mechanisms that govern the partitioning between seismic and aseismic slip and their interaction remain unclear. Here we present a numerical modeling study of earthquake sequences and aseismic transient slip on oceanic transform faults. In the model, strong dilatancy strengthening, supported by seismic imaging that indicates enhanced fluid-filled porosity and possible hydrothermal circulation down to the brittle–ductile transition, effectively stabilizes along-strike seismic rupture propagation and results in rupture barriers where aseismic transients arise episodically. The modeled slow slip migrates along the barrier zones at speeds ∼10 to 600 m/h, spatiotemporally correlated with the observed migration of seismic swarms on the Gofar transform. Our model thus suggests the possible prevalence of episodic aseismic transients in M ∼ 6 rupture barrier zones that host active swarms on oceanic transform faults and provides candidates for future seafloor geodesy experiments to verify the relation between aseismic fault slip, earthquake swarms, and fault zone hydromechanical properties.

oceanic transform faults | earthquake rupture segmentation | aseismic transients | seismic swarms

Averaged globally, oceanic transform faults (OTFs) release a small percentage (∼15%) of their accumulated moment seismically, and despite the large thermally defined potential rupture area the largest observed earthquakes have only moderate magnitudes (up to magnitude 7 [M7]) (1, 2). Recent ocean bottom seismometer (OBS) deployment experiments along OTFs associated with fast-spreading ridges provide near-field seismic data that shed light on the source mechanism of OTF earthquake rupture patterns and possible interaction between aseismic and seismic slip modes (3–7). On the Gofar transform of the East Pacific Rise (EPR), M ∼ 6 earthquakes repeat quasi-periodically every 5 to 6 y on 15- to 20-km along-strike segments separated by a ∼10-km barrier zone (8). The rupture pattern is inferred from the 2008 foreshock and aftershock distributions (3) (Fig. 1) and the relative centroid locations of M6.0+ events on Gofar since 1992 (2, 8). Similar earthquake rupture patterns are observed along the Blanco Ridge transform of the northeast Pacific Ocean, where a ∼10-km barrier zone separates two distinctive moment magnitude (M_w) 6.0 to 6.5 patches that rupture quasi-periodically every ∼14 y (2, 7). Repeated ruptures are also reported on transforms that offset slow-spreading ridges, such as the Charlie-Gibbs transform of the Mid-Atlantic Ridge (9), although large location uncertainties exist using teleseismic data.

The persistent rupture barrier through multiple cycles, recent OBS-based observations of the fine-scale seismicity distribution (3), and fault zone velocity structure on Gofar (5) jointly suggest that the material properties of the barrier zone are distinct from those in the M ∼ 6 rupture zones. Prior to the 2008 M_w 6.0 mainshock, the central barrier zone experienced ∼22,000 foreshocks (M0 to 4.5) extending in depth to the uppermost mantle, likely a few kilometers deeper than the lower limit of oceanic crustal seismicity defined by the 600 °C isotherm (10). An active-source refraction line across the barrier zone revealed ∼10 to 20% reduction in P-wave velocities in a several-kilometer-wide damage zone extending through the entire oceanic crust (5), in contrast to a nearly intact fault zone in the fully coupled mainshock area (4). Systematically lower static stress drop values are also estimated for earthquakes in the barrier zone (11), which are consistent with the seismic velocity reduction. Significant (up to ∼50%) seismic velocity reduction is also common along continental transform faults and is usually attributed to a mechanical damage zone due to intense fracturing (12). The depth extent of continental low-velocity zones is less clear and it may not extend all of the way to the brittle–ductile transition as observed on the Gofar fault (5). This large velocity anomaly on Gofar can be achieved by either enhanced fluid-filled porosity of 1.5 to 8% or a large volume fraction of mineral alternation at crustal depths (e.g., 50 to 90% altered peridotite or >70% serpentinized troctolite) (5). However, such large-scale alternation would produce

Significance

Oceanic transform faults slip through a unique combination of seismic and aseismic behavior. But the geological conditions and physical mechanisms that lead to different slip modes on different parts of the same fault remain unresolved. Recent seafloor experiments document abundant microseismicity in barrier zones that separate large earthquake ruptures. These barriers require an explanation that permits small earthquake nucleation, but prohibits large rupture propagation. We find that coupling frictional dilatancy to a physics-based earthquake cycle model can simultaneously reproduce the rupture segmentation and slip partition observed on the Gofar transform fault, East Pacific Rise. Our model shows a prevalence of slow slip events that drive migrating microearthquake swarms, a prediction that can be tested with future seafloor geodesy experiments.

Author contributions: Y.L. designed research; Y.L. and J.J.M. performed research; Y.L. and J.J.M. analyzed data; and Y.L., J.J.M., and M.D.B. wrote the paper.

The authors declare no competing interest.

This article is a PNAS Direct Submission.

Data deposition: Seismic waveform data from the 2008 Gofar ocean bottom seismometer experiment are archived at the Incorporated Research Institutions for Seismology (IRIS) data center, network code ZD, https://www.fdsn.org/networks/detail/ZD_2007/. Data products can be accessed on Open Science Framework at https://osf.io/rw9bq/.

[1]To whom correspondence may be addressed. Email: yajing.liu@mcgill.ca.

This article contains supporting information online at https://www.pnas.org/lookup/suppl/doi:10.1073/pnas.1913625117/-/DCSupplemental.

First published April 28, 2020.

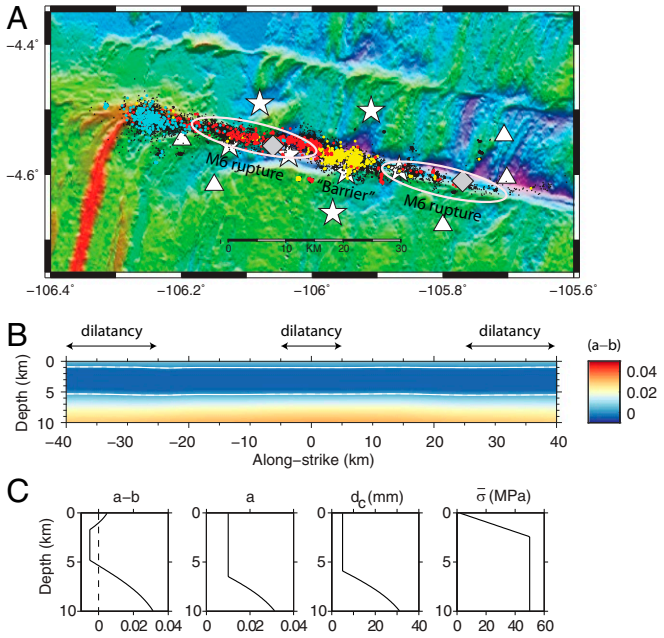

Fig. 1. Gofar transform fault seismicity, M6 rupture segments, and earthquake cycle model setup. (*A*) Seismicity was recorded and located in August to December 2008 (black dots), surrounding an M_w 6 mainshock on September 18, 2008. Yellow, foreshocks on September 10 to 12; red, aftershocks on September 18 to 20; cyan, swarm seismicity on December 7 to 8. White triangles, seismometer; white stars, seismometer colocated with strong-motion sensor. White ellipses show the estimated rupture extents of the 2008 M_w 6 (west) and 2007 M_w 6.2 (east), with gray diamonds denoting respective centroid locations. Image credit: modified from McGuire et al. (3). (*B*) Rate–state friction stability parameter ($a-b$) mapped on the transform fault representing western Gofar. Area within two white lines (friction stability transition, $a-b=0$) has velocity-weakening friction ($a-b<0$); outside is velocity strengthening ($a-b>0$). (*C*) Depth distributions of friction parameters $a-b$, a, characteristic slip distance d_c, and effective normal stress $\bar{\sigma}$.

a gravity anomaly much greater than that observed across the Gofar barrier zone, whereas the estimated porosity change would produce a gravity signature below the measurement sensitivity (5). Therefore, enhanced fluid-filled porosity is likely the primary mechanism for the seismic velocity reduction in the barrier zone on Gofar.

Precise seismicity relocation on western Gofar identified a ∼600-m fault trace offset at the boundary between the 2008 M_w 6.0 rupture and the barrier zone (Fig. 1), which spatially coincides with a ∼500-m-deep seafloor depression (4). Although a fault trace offset <1 km is not likely to be sufficient to stop a M_w 6.0 dynamic rupture based on observations from continental transform faults (13, 14), such local complexity in the fault geometry provides favorable conditions for normal faulting and fluid infiltration, in a manner similar to that of a pull-apart basin (15). Hydrothermal circulation is also likely responsible for lowering the fault zone temperature and hence increasing the depth of the brittle–ductile transition into the upper mantle, where pervasive serpentinization is suggested to favor aseismic slip and promote abundant earthquake swarms, as recently observed along the Blanco Ridge transform (7, 16). The persistent supply of excess fluids can result in large fluid-filled porosity and high pore pressure, both of which can influence fault slip behavior.

In fluid-saturated granular materials, porosity evolves as shear begins (17, 18). If the shear sliding rate, and consequently the rate of creating new void space by rotating and fracturing grains, is more rapid than ambient fluids can flow into the new pore space, local pore pressure is temporally reduced and effective normal stress (normal stress minus pore pressure) is enhanced. This dilatancy-strengthening mechanism has been proposed to be effective in inhibiting dynamic deformation in landslides, glacier tills, and fault gouges (17–19) and more recently in numerical models generating episodic slow slip events in subduction zones (20, 21). Based on the aforementioned observational evidence, we investigate the feasibility of dilatancy strengthening as a mechanism for the persistent rupture barrier behavior on the Gofar transform and its implications for the oceanic transform fault slip budget.

OTF Earthquake Sequence Model Coupled with Dilatancy

We develop a three-dimensional (3D) numerical model based on the Gofar transform, including OTF-specific loading and boundary conditions, to simulate earthquake rupture sequences on the western Gofar fault segment governed by laboratory-derived rate- and state-dependent friction laws (22). In the rate–state framework, the friction stability parameter $a-b$ dictates to the first order whether slip has the potential to grow into a seismic event ($a-b<0$, velocity weakening [VW]) or will remain stable ($a-b>0$, velocity strengthening [VS]) (23, 24) (*Materials and Methods*). In our model, $a-b$ is mapped on the OTF by converting temperature-dependent gabbro gouge rate–state friction data (25) using a western Gofar thermal structure calculated with hydrothermal cooling and visco-plastic rheology (10). Seismic slip can be achieved when the down-dip dimension of the VW segment exceeds a characteristic nucleation size defined by the friction, normal stress, and pore pressure conditions on the fault (*Materials and Methods*). In the model presented here, the above instability condition is always satisfied such that the entire ∼4-km (1 to 5 km in depth) VW zone ruptures in a single earthquake without an effective stabilizing mechanism (*SI Appendix*, Fig. S1).

The stable–unstable competition dictated by the VS–VW properties can be used to design spatial distributions of $a-b$, along with other model parameters, such that earthquake ruptures are mainly confined within the VW zones. For example, in numerical models consisting of homogeneous, alternating VS/VW segments, a larger VS zone, higher effective normal stress, and larger $a-b$ values are all favorable conditions for inhibiting the propagation of seismic ruptures that originated from the neighboring VW segments (26). For Gofar, we find that when a 10-km along-strike VS zone is embedded between two 20-km VW zones, M6 ruptures in the VW zones do not propagate into the central VS zone, resulting in a rupture barrier (*SI Appendix*, Fig. S2; all other parameters the same as in the *SI Appendix*, Fig. S1 case). However, such a crustal-scale VS zone is unlikely because fault zone temperature there is largely lower than ∼500 °C required for $a-b>0$ based on laboratory gabbro friction data (25) and pervasive serpentinization appears unlikely as discussed above. The occurrences of ∼20,000 foreshocks in the barrier zone to the 2008 M_w 6.0 also suggest that the entire oceanic crust cannot simply slip aseismically under VS conditions.

More complex spatial heterogeneities, such as random or stochastic distributions of $a-b$, can also be introduced to generate small earthquakes on VW patches embedded in a largely VS, creeping background. Such a VW–VS mélange can work effectively to stop M6 ruptures from adjacent segments, as best illustrated by the arrest of Parkfield earthquake ruptures at the creeping section along the central San Andreas Fault (27). Within the San Andreas Fault creeping section, VW friction appears to be limited to small areas along the streaks of microseismicity (28), therefore leaving the majority of the fault area at VS. By contrast, the western Gofar barrier zone is spectacularly seismically active, generating thousands of microearthquakes per week in a short 10-km fault segment (3). The abundant and widespread distribution of microseismicity in the western Gofar barrier zone and its adjacency to the M6 mainshock zone strongly

suggest, if such a VW–VS mélange is present, that the VW patches predominate and are separated only by sporadic VS patches. Despite this predominance of VW material, the barrier zone repeatedly stops large ruptures (3). This proportionality would be analogous to the stochastic VW–VS distribution in the transition zone at the bottom of the seismogenic layer proposed to reconcile seismicity and geodetic locking depths on the Anza section of the San Jacinto Fault (29). As numerically demonstrated for Anza (29), under such a frictional stability parameter distribution, an earthquake rupture nucleated from the large VW seismogenic zone would still propagate through the VW–VS mixture, inconsistent with the rupture barrier observation here on Gofar.

Thus to construct a model consistent with these field observations and numerical predictions in previous studies, dilatancy strengthening is introduced on three along-strike segments of the fault, 10 km at the center and 15 km on each end; fault properties elsewhere are not modified (Fig. 1*B*). Such an along-strike distribution of dilatancy is chosen to spatially reflect the M $\sim$ 6.0 rupture patterns on western Gofar (Fig. 1*A*), which allows us to determine whether dilatancy can effectively stop the ruptures given the plausible porosity values inferred from the P-wave anomaly in the barrier zone (5). There are two key dilatancy parameters in our model setting. The first parameter is the nondimensional dilatancy coefficient ϵ, which measures porosity changes with shear velocity steps. A higher ϵ corresponds to a larger increase in porosity for a given increase in sliding velocity and hence greater tendency for slip stabilization and arrest; ϵ is between 10^{-5} and 10^{-4} measured in fault sliding experiments on natural and simulated gouges (19, 30, 31). The second parameter is the bulk porosity ϕ, which varies between 0.01 and 0.1 as inferred for the Gofar rupture barrier zone (5). Pore pressure evolution, controlled by frictional slip along the fault and fluid diffusion across the fault, is coupled to the rate–state friction framework to obtain the spatiotemporal evolution of slip rate, shear stress, and pore pressure on the entire fault (19, 20) (*Materials and Methods*).

Rupture Barrier

Fig. 2 *A* and *B* shows a ~10-y history of slip and slip rate for a simulation case with porosity $\phi = 0.05$ and dilatancy coefficient $\epsilon = 10^{-4}$, which are in the range of parameters estimated for western Gofar (see *SI Appendix*, Figs. S1 and S3, for additional simulation cases with other values of ϕ and ϵ). In contrast to a whole-fault rupture as predicted with no or a weak dilatancy effect ($\epsilon = 10^{-5}$; *SI Appendix*, Fig. S1), earthquake rupture in the model with zones of strong dilatancy is separated into western and eastern segments, repeating every 5 to 6 y (Fig. 2 *A* and *B*). Coseismic rupture initiates at the boundaries of strong-dilatancy to no-dilatancy zones, and propagation is mainly contained within the no-dilatancy zone with quickly diminishing rupture speeds approaching the boundaries on either side. As a result, the central dilatancy zone (-5 to 5 km) becomes a rupture barrier to M $\sim$ 6 events on each side. The other two dilatancy zones at the western and eastern ends of the fault also remain aseismic. The pair of modeled M $\sim$ 6 ruptures follows a general pattern where the seismic cycles of the two rupture patches have similar phasing such that the M $\sim$ 6 ruptures often happen within a few months of each other, similar to the westward sequence of rupture observed on Gofar in the past earthquake cycles (8).

We further quantify the seismic coupling ratio (χ_s) within the central barrier zone as a function of the degree of dilatancy, represented by the nondimensional parameter ϵ/ϕ (Fig. 2*C*; see

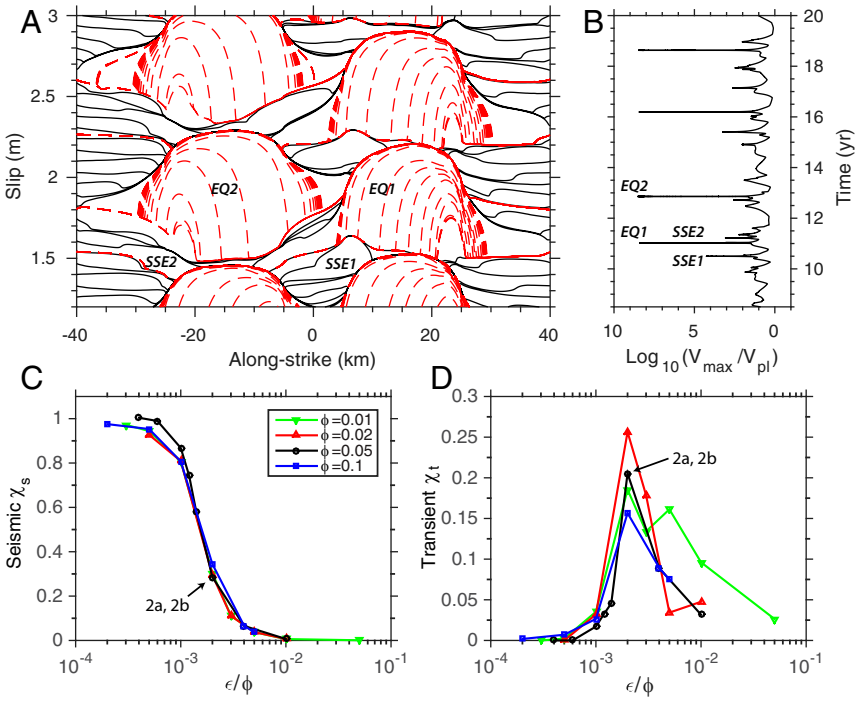

Fig. 2. Modeled earthquake rupture pattern and aseismic vs. seismic slip budget. (*A*) Cumulative slip in multiple earthquake cycles at depth 4 km. Black solid lines are interseismic slip ($V_{max} < 10^6 V_{pl}$) plotted every 0.5 y. Red dashed lines are coseismic slip ($V_{max} \geq 10^6 V_{pl}$) plotted every second. Plate loading rate $V_{pl} = 14$ cm/y. (*B*) Normalized maximum slip rate $\log_{10}(V_{max}/V_{pl})$ on the fault for the same period as in *A*. SSE1 and SSE2 denote the timing and locations of two aseismic slip transients; EQ1 and EQ2 denote two earthquakes. $\phi = 0.05$, $\epsilon = 10^{-4}$ for the case in *A* and *B*. (*C*) Fraction of slip released during seismic events χ_s, averaged over the modeled earthquake cycles and within the central high dilatancy zone (-5 to 5 km) under different dilatancy conditions, represented by the ratio between dilatancy coefficient and porosity ϵ/ϕ. (*D*) Fraction of aseismic transient slip χ_t averaged over multiple earthquake cycles and within the central high-dilatancy zone. Black arrows in *C* and *D* point to the simulation case shown in *A* and *B*.

Materials and Methods for the formulation of ϵ/ϕ). Here χ_s is defined as the ratio of slip released seismically to the total slip accumulated at the full loading rate ($V_{pl} = 14$ cm/y) in multiple modeled earthquake cycles (*Materials and Methods*). For example, for the case in Fig. 2*A* ($\epsilon/\phi = 0.002$), about 30% of the total moment is released seismically in the barrier zone, as a result of coseismic slip propagating into it prior to a complete stop. Overall, the coupling ratio decreases with increasing ϵ/ϕ or, equivalently, greater dilatancy effect. Our results thus confirm the hypothesis that dilatancy strengthening can serve as an effective mechanism for arresting seismic slip and result in rupture barriers to M $\sim$ 6 earthquakes as observed along western Gofar.

Aseismic Slip Transients Driving Seismic Swarms

The central barrier zone does not slip simply at, or below, the plate loading rate V_{pl}. Rather, this region experiences transient aseismic slip events, as illustrated in Fig. 2*B*, with excursions in slip rate one to three orders of magnitude above V_{pl} during the intervening periods between the M $\sim$ 6 earthquakes. Here we quantify the aseismic transient slip ratio χ_t as fault slip that would exceed the geodetic detection threshold (several times V_{pl}) but is not associated with earthquakes (i.e., excluding earthquake nucleation and coseismic and postseismic phases) (*Materials and Methods*). In contrast to the seismic coupling ratio χ_s, which monotonically decreases with an increasing dilatancy effect (Fig. 2*C*), χ_t is greatest for the choices of porosity and dilatancy coefficient pairs that result in an intermediate value $\epsilon/\phi = 0.002$ (Fig. 2*D*); a weaker dilatancy effect is not sufficient to stabilize seismic slip to aseismic transients whereas a stronger effect leads to slip rates near or lower than V_{pl} (*SI Appendix*, Fig. S3). Within the intermediate range of ϵ/ϕ, the average χ_t in the central barrier zone can reach 15 to 25%, a significant fraction of the total OTF slip budget.

The transient slip events nucleate at the peripherals of the locked M $\sim$ 6 rupture zones and propagate across the adjacent rupture barrier zones at a speed of 10 to 600 m/h within $\sim$5 to 10 d. Propagation speeds average $\sim$100 m/h for the events in the central barrier zone (Fig. 3) and $\sim$20 m/h for the events in the west-end barrier zone (*SI Appendix*, Fig. S4). Both cases are simulated with $\epsilon = 10^{-4}$ and $\phi = 0.05$. Fig. 4 shows the December 2008 swarm events, the most abundant swarm episode during the 2008 Gofar OBS experiment, on the westernmost segment of Gofar (cyan dots in Fig. 1*A*, longitude -106.2 to $-106.3°$S). The seismicity migration envelope can be accurately described by the propagation of modeled aseismic slip transients with a range of dilatancy coefficients $\epsilon = (0.7 \text{ to } 1.2) \times 10^{-4}$ and a porosity of $\phi = 0.05$. Note that this range of $\epsilon/\phi = (1.4 \text{ to } 2.4) \times 10^{-3}$ corresponds to the peak aseismic transient slip budget (χ_t) as shown in Fig. 2*D*.

The aseismic slip propagation fronts in general follow a diffusional curve, with faster migration in the first 1 to 2 d followed by slower speeds for the remaining period. The average migration speed does not vary much for the range of dilatancy parameters that produce significant transient slip; clear migration patterns are difficult to quantify for cases outside the peak χ_t range due to lower slip rates and smaller slip areas. We propose that aseismic transient slip may be the driving mechanism for seismicity swarms on Gofar, such as inferred for continental strike-slip faults (32) and subduction zones (33), and possibly a manifestation of porosity wave migration within the rupture barrier. Although no transient slip events have been detected geodetically along OTFs due to lack of instrumentation, their appearance in our numerical model and similar migration pattern to the Gofar swarms suggest they may be a common mode of slip along oceanic transform faults and a prevalent slip mechanism within OTF rupture barriers. Distinct from the slow slip events observed in subduction zones

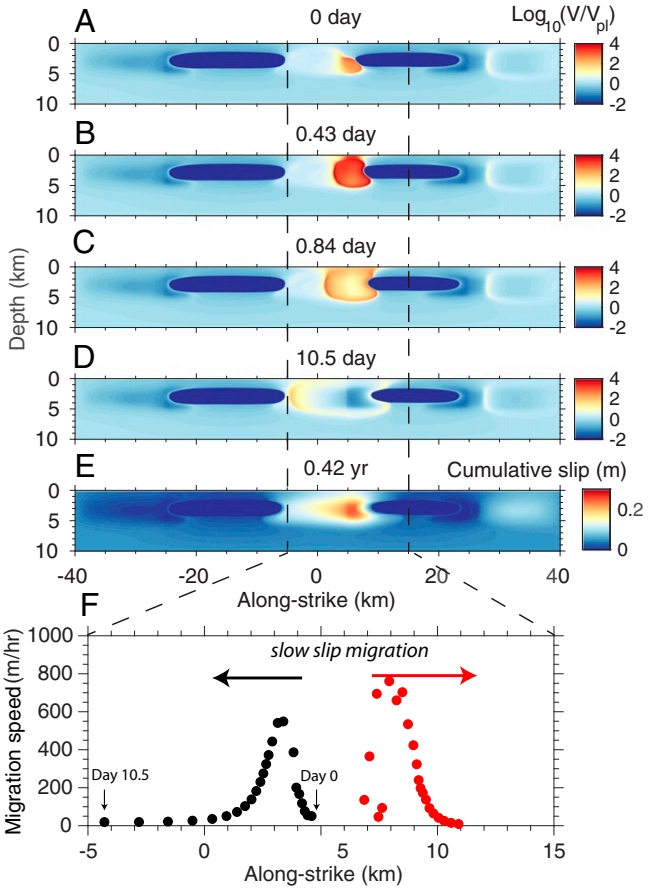

Fig. 3. Modeled aseismic transient slip propagation (SSE1 in Fig. 2 *A* and *B*). (*A–D*) Snapshots of normalized slip rate on the fault at times 0, 0.43, 0.84, and 10.5 d from a reference starting time $t = 10.5$ y as shown in Fig. 2*B*. Red/orange colors represent migrating transient slip at rates between $\sim V_{pl}$ and $10^4 V_{pl}$. Dark blue areas represent locked segments that previously ruptured in M $\sim$ 6 earthquakes. (*E*) A total of maximum 30 cm slip accumulated in 0.42 y (t = 10.26 to 10.68 y), defined as the duration of this episode when $V_{max} > 10^{0.8} V_{pl}$. (*F*) Westward and eastward aseismic transient slip front migration speeds during the active 10.5-d period shown in *A–D*. The central high-dilatancy zone is defined within along-strike -5 to 5 km. Dilatancy coefficient $\epsilon = 10^{-4}$, porosity $\phi = 0.05$.

(34, 35), the maximum cumulative slip in each aseismic slip episode can reach $\sim$30 cm (Fig. 3*E*), with surface displacements up to $\sim$10 cm (*SI Appendix*, Fig. S6), rendering a unique test of the dilatancy hypothesis by future seafloor geodesy experiments.

Discussion and Conclusions

Hypotheses proposed to explain the partitioning between aseismic and seismic slip on oceanic transform faults essentially involve either a single-mode or a multimode rupture scenario. In the single-mode scenario, earthquakes persistently occur on fully coupled segments of distinct frictional properties due to spatially variable lithology and degree of hydration (3, 8). In the multimode rupture scenario, fault segments transition between aseismic and seismic slip modes as either frictional properties evolve over time due to changes in fault hydromechanical conditions (36) or the dimensional ratio between the seismogenic zone and the characteristic nucleation zone (defined in the rate–state framework) leads to a mixture of aseismic and seismic slip (22). The quasi-periodic occurrences of M_w 5 to 6 earthquakes with similar centroid locations on the Gofar-Discovery and Blanco Ridge transform faults

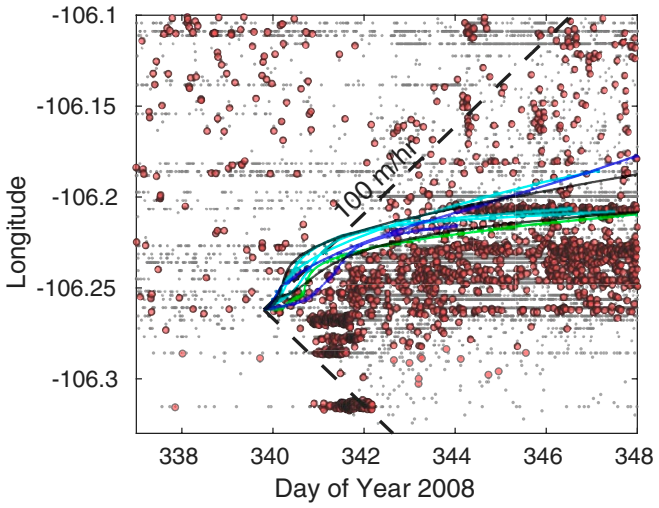

Fig. 4. Seismic swarm in December 2008 and modeled aseismic slip migration fronts. Red dots show relocated M ~1 to 3 earthquakes detected within ~10 d near the Gofar transform–ridge interaction toward the west end. Gray dots show matched-filter–based detections of smaller events (M0 to 2) that were not relocated independently from their template (3). Black dashed line shows a linear migration speed at 100 m/h, for reference. Solid lines show modeled diffusive aseismic slip fronts from simulation cases using porosity $\phi = 0.05$ and dilatancy coefficient $\epsilon = 0.7 \times 10^{-4}$ (cyan, three cases), 0.8×10^{-4} (blue, two cases), 10^{-4} (black, two cases), and 1.2×10^{-4} (green, one case).

(7, 8) are more consistent with the single-mode pattern. The OTF slip evolution modeled in our study after Gofar clearly demonstrates that strong dilatancy can stop seismic rupture propagation and result in persistent rupture barrier zones as observed for the Gofar transform. For the Blanco Ridge transform, fault geometry and bathymetry changes may play more important roles in the M_w 6.0 to 6.5 central barrier zone (7), where the occurrence of a local magnitude 5.5 indicates possibly higher fault strength and weaker dilatancy effect than those in the barrier zones along Gofar. Future studies on oceanic transform fault geometry, velocity structure, and high-precision seismicity location are needed to determine to what extent the dilatancy mechanism affects global OTFs' earthquake rupture patterns.

Our modeling results also suggest a two-way stress triggering between aseismic creep in the high-dilatancy, rupture barrier zones and the M ~ 6 in the coupled seismogenic zones. Strain energy release from an aseismic transient slip event in the barrier zone increases stresses around the peripherals of the slip zone and promotes earthquake nucleation in the neighboring segments. Coseismic and postseismic slip in the M ~ 6 rupture zones consequently increases loading on the adjacent barrier zones and leads to aseismic transients (Fig. 2 *A* and *B*). We note from Fig. 2*B* that not all aseismic transient slip events precede an earthquake rupture, which suggests that the stress state of the future seismogenic zone must be taken into consideration.

Seismic swarm activity has been long recognized on plate boundary faults (37–39) and is suggested to be a manifestation of brittle failure on small asperities driven by aseismic creep in the crust or upper mantle layers (7, 40). Swarm migration characteristics thus provide useful insights into the underlying fault slip behavior. A recent study using ocean bottom seismometers deployed near the Blanco Ridge found consistent swarm migration rates from 100 to 2,000 m/h with a median of 370 m/h (7). A wide range of swarm migration speed is also found for western Gofar. For the December 2008 swarm episode on the west end of Gofar (Fig. 4), seismicity propagates on average at ~20 to 100 m/h over a period of about 1 wk, at least an order of magnitude slower than those on the Blanco transform fault. Several other swarm episodes are also identified with migration speeds <1,000 m/h from the relocated epicenters (*SI Appendix*, Fig. S7) (4), although the event numbers of each episode are far fewer than those in the December 2008 episode. Furthermore, the Blanco swarms demonstrate a roughly linear migration pattern (7), whereas the majority of the Gofar December 2008 swarm sequence followed an approximately diffusive curve (Fig. 4, solid lines). The Gofar swarm migration speed and pattern are indeed more comparable to those of seismic bursts in southern California exhibiting migration indicative of fluid diffusion (41). The above differences in the Gofar and Blanco swarm migration characteristics may suggest different degrees of fluid involvement. Hydrothermal circulation and the minor extent of mineral alternation (10) combine to enhance porosity and hence dilatancy effect in the Gofar rupture barrier zones, thereby promoting aseismic transient slip and driving diffusional swarm migration at crustal depths. By contrast, pore space in the Blanco mantle layer may be primarily filled by serpentine, such that little to no dilatancy effect is exhibited nor are diffusional patterns of swarm migration observed.

The presence of abundant aseismic slip, evolving in time and space, has fundamental implications for the type of earthquake sequences and total slip budget on major plate boundary faults. Future work is required to understand how aseismic slip leads to seismic swarms, sometimes in the form of repeating microearthquakes, as has been reported in several cases preceding large megathrust earthquakes (42, 43). The potential stress triggering between aseismic creep, seismic swarms, and subsequently large earthquakes may allow us to better understand the earthquake nucleation process that has long evaded seismologists.

Materials and Methods

Rate–Station Friction Coupled with Dilatancy. We implement the laboratory-derived rate- and state-dependent friction law (23), coupled with dilatancy (19), to simulate fault slip (δ), shear stress (τ), and pore pressure (p) evolution in OTF earthquake cycles, following

$$\tau = \bar{\sigma} f = (\sigma - p)\,[f_0 + a \ln(V/V_0) + b \ln(V_0 \theta / d_c)], \quad [1]$$

$$\frac{d\theta}{dt} = 1 - \frac{V\theta}{d_c}, \quad [2]$$

$$\frac{dp}{dt} = -\frac{p - p_0}{t_p} + \frac{\epsilon}{\beta}\frac{1}{\theta}\frac{d\theta}{dt}, \quad [3]$$

where θ is the state variable. Effective normal stress $\bar{\sigma} \equiv \sigma - p$, and rate–state friction parameters a, b, d_c are time constant but spatially variable. Reference slip rate $V_0 = 10^{-6}$ m/s, and nominal friction coefficient $f_0 = 0.6$ when $V = V_0$. The earthquake nucleates on a velocity-weakening ($a - b < 0$) fault of a dimension greater than the characteristic nucleation size defined as $h^* = \gamma \frac{\mu b d_c}{(b-a)^2 \bar{\sigma}}$ (44), where μ is shear modulus, and γ is a geometrical factor of unity. We adopt laboratory measurement of temperature-dependent friction stability parameter $a - b$ for gabbro gouge under hydrothermal conditions (25) and convert it to be depth-dependent (Fig. 1) using a Gofar thermal model (10) that accounts for hydrothermal circulation effect. $\bar{\sigma} = 50$ MPa and the characteristic slip distance d_c is ~5 mm such that the width of the seismogenic zone ($W \sim 4$ km) is about 3.5 times that of the nucleation zone $h^* \sim 1.14$ km, under which nearly all slip is released in earthquakes (22).

The elastic relation between slip δ and shear stress τ follows the "quasi-dynamic" approximation (45)

$$\tau(x, \xi, t) = -\int_0^{x_L}\int_0^{W_d} k(x - x', \xi, \xi')\,[\delta(x', \xi', t) - V_{pl} t]\,dx'd\xi' - \eta\frac{\partial \delta(x, \xi, t)}{\partial t}, \quad [4]$$

where $X_L = 80$ km and $W_d = 10$ km are the along-strike and along-dip dimensions of the modeled OTF, respectively. The stiffness matrix $k(x - x', \xi, \xi')$ represents shear stress change at location (x, ξ) due to a unit slip at location (x', ξ'), where a Fourier transform is applied along the strike (x) to account for translational symmetry and reduce computation time.

In Eq. **3**, $t_p \equiv \eta\beta d^2/k$ is the characteristic diffusion timescale for fault zone pore pressure p to reequilibrate with the ambient pressure p_0 across a fault zone of finite thickness d (19). It is challenging to estimate t_p because fault zone thickness d and permeability k are largely unknown for Gofar. A plausible range of $k \approx 10^{-14}$ to 10^{-20} m^2 for $d \sim 1$ mm (fault core) to $\sim$1 m (damage zone) (46) results in a wide range of $t_p \approx 10^9\phi$ to $10^{-3}\phi$ [s], where ϕ is fault zone porosity and $\beta = \phi(\beta_f + \beta_\phi)$ is fault gouge bulk compressibility, defined with fluid compressibility $\beta_f = 5 \times 10^{-4}$ MPa^{-1}, solid compressibility $\beta_\phi = 10^{-2}$ MPa^{-1}, and fluid dynamic viscosity $\eta = 10^{-3}$ Pa·s. At intermediate drainage conditions, for example, $t_p \approx 10^3\phi$, for $\phi =$ 0.01 to 0.1, as inferred for the rupture barrier zone of Gofar (5), $t_p \approx 10$ to 100 s, which is comparable to the coseismic rupture timescale, meaning that any pore pressure change would nearly instantaneously return to its ambient level (effectively drained), equivalent to no dilatancy effect. Furthermore, previous numerical studies have found that at intermediate drainage conditions, $t_p/(d_c/V_{pl}) \approx 0.01$ to 0.1, the total coseismic slip and rupture depth range of modeled earthquakes are similar to their reference values without dilatancy (22). Therefore, in this study we focus on the nearly undrained condition of $t_p \approx 10^9\phi$, which maximizes the dilatancy effect; this is equivalent to assuming $k = 10^{-20}$ m^2 within $d = 1$ mm. With the above assumptions, the controlling parameters to pore pressure evolution (Eq. **3**) are ϵ and ϕ, which enter the second term in Eq. **3** as their ratio ϵ/ϕ.

Small perturbations are introduced into the initial conditions to allow the system to evolve off steady state and into nonuniform slip mode. Specifically, at the beginning of each simulation, $t = 0$ y, we set state variable $\theta = d_c/V_{pl}$ (steady state) everywhere on the fault, except for the segment between -25 to -5 km along strike; $\theta = d_c/(2.5V_{pl})$ on that segment. V, θ, and p evolutions become independent of the initial conditions after the first cycle of earthquakes.

OTF Slip Budget. We use the maximum fault slip rate V_{max} as a criterion to quantify seismic versus aseismic slip. Slip is defined as seismic (χ_s) when $V_{max} \geq 5$ mm/s $\approx 10^6 V_{pl}$ and aseismic (χ_a) when $10^{0.8}V_{pl} < V_{max} < 10^6 V_{pl}$, and a subset of aseismic slip during periods not associated with earthquakes, i.e., excluding slip in earthquake nucleation and postseismic phases, is quantified as transient slip (χ_t). Lower cutoff velocities, $10^{0.5}V_{pl}$ and $10^{0.3}V_{pl}$, are also tested, and the overall slip budget dependence on dilatancy parameters as in Fig. 2 *C* and *D* and *SI Appendix*, Fig. S3 is not affected. χ_s, χ_a, and χ_t are all calculated as the ratio of slip released in respective phases to the total slip accumulated in the seismogenic zone (velocity weakening) over multiple OTF earthquake cycles, typically $\sim$10 cycles when the coupling coefficients reach long-term steady-state values (22). *SI Appendix*, Fig. S3 shows the along-strike distribution of χ_s, χ_a, and χ_t slip ratios as the effect of dilatancy varies from weak to strong, $\epsilon = (0.2, 0.3, 0.5, 0.6, 0.7, 1, 2, 5) \times 10^{-4}$ (light gray to dark lines), with a constant porosity value $\phi = 0.05$. We can see a clear locking effect under strong dilatancy $\epsilon = 2 \times 10^{-4}$ and 5×10^{-4}, the latter shown in red, in the central $\sim$10 km and $\sim$15 km at each of the two ridge–transform intersections. Aseismic slip is in general complementary to the seismic slip budget, but the two modes of slip do not necessarily add up to 1 in the three segments with strong dilatancy, because a significant portion is released when $V_{max} < 10^{0.8}V_{pl}$, which accounts for extremely slow creep during the interseismic loading period.

Aseismic Transient Migration. Colored solid lines in Fig. 4 show the migration fronts of aseismic transient events modeled with $\phi = 0.05$ and $\epsilon =$ 0.7 to 1.2 $\times 10^{-4}$ (a total of eight simulation cases). The origin of these modeled diffusional fronts is set at day 339.8 and longitude 106.262°S, assuming one longitudinal degree is 105 km, for a direct comparison to the Gofar swarm migration at the same spatial and temporal scales. For each snapshot, the east and west fronts of the bilateral slip migration are respectively defined as the eastern- and western-most positions on the contour line where slip velocity is a fraction (e.g., 0.8) of the maximum velocity V_{max} on the fault of that snapshot. Several fraction thresholds in the range of 0.6 to 0.85 are tested and the migration front positions are not strongly affected (*SI Appendix*, Fig. S5).

Data Availability. Seismic waveform data from the 2008 Gofar ocean bottom seismometer experiment are archived at the Incorporated Research Institutions for Seismology (IRIS) data center, network code ZD, https://www.fdsn.org/networks/detail/ZD_2007/. Data products can be accessed on Open Science Framework at https://osf.io/rw9bq/.

ACKNOWLEDGMENTS. We thank Joan Gomberg, Ruth Harris, Steve Hickman, Shane Detweiler, Mike Diggles, and two anonymous external reviewers for their thoughtful comments that helped to improve the manuscript. This study was supported by Natural Sciences and Engineering Research Council of Canada Discovery Grants RGPIN/418338-2012 and RGPIN-2018-05389; and NSF Grants OCE-10-61203 and OCE-18-33279.

1. M. S. Boettcher, T. H. Jordan, Earthquake scaling relations for mid-ocean ridge transform faults. *J. Geophys. Res.* **109**, B12302 (2004).
2. M. S. Boettcher, J. J. McGuire, Scaling relations for seismic cycles on mid-ocean ridge transform faults. *Geophys. Res. Lett.* **36**, L21301 (2009).
3. J. McGuire *et al.*, Variations in earthquake rupture properties along the Gofar transform fault, East Pacific Rise. *Nat. Geosci.* **5**, 336–341 (2012).
4. B. Froment *et al.*, Imaging along-strike variations in mechanical properties of the Gofar transform fault, East Pacific Rise. *J. Geophys. Res.* **119**, 7175–7194 (2014).
5. E. Roland, D. Lizarralde, J. McGuire, J. Collins, Seismic velocity constraints on the material properties that control earthquake behavior at the Quebrada-Discovery-Gofar transform faults, East Pacific Rise. *J. Geophys. Res.* **117**, B11102 (2012).
6. M. Wofson-Schwehr, M. Boettcher, J. McGuire, J. Collins, The relationship between seismicity and fault structure on the Discovery transform fault, East Pacific Rise. *Geochem. Geophys. Geosyst.* **15**, 3698–3712 (2014).
7. V. M. Kuna, J. L. Nabelek, J. Braunmiller, Mode of slip and crust-mantle interaction at oceanic transform faults. *Nat. Geosci.* **12**, 138–142 (2019).
8. J. McGuire, Seismic cycles and earthquake predictability on East Pacific Rise transform faults. *Bull. Seismol. Soc. Am.* **98**, 1067–1084 (2008).
9. K. Aderhold, R. E. Abercrombie, The 2015 Mw 7.1 earthquake on the Charlie-Gibbs transform fault: Repeating earthquakes and multimodal slip on a slow oceanic transform. *Geophys. Res. Lett.* **43**, 6119–6128 (2016).
10. E. Roland, M. Behn, G. Hirth, Thermal-mechanical behavior of oceanic transform faults: Implications for the spatial distribution of seismicity. *Geochem. Geophys. Geosys.* **11**, Q07001 (2010).
11. P. A. Moyer, M. S. Boettcher, J. J. McGuire, J. A. Collins, Spatial and temporal variations in earthquake stress drop on Gofar Transform Fault, East Pacific Rise: Implications for fault strength. *J. Geophys. Res.* **123**, 7722–7740 (2018).
12. E. S. Cochran *et al.*, Seismic and geodetic evidence for extensive, long-lived fault damage zones. *Geology* **37**, 315–318 (2009).
13. S. G. Wesnousky, Seismological and structural evolution of strike-slip faults. *Nature* **335**, 340–343 (1988).
14. G. P. Biasi, S. G. Wesnousky, Steps and gaps in ground ruptures: Empirical bounds on rupture propagation. *Bull. Seismol. Soc. Am.* **106**, 1110–1124 (2016).
15. P. M. Gregg, J. Lin, D. K. Smith, Segmentation of transform systems on the East Pacific Rise: Implications for earthquake processes at fast-slipping oceanic transform faults. *Geology* **34**, 289–292 (2006).
16. J. J. McGuire, The geology of earthquake swarms. *Nat. Geosci.* **12**, 82–87 (2019).
17. C. Marone, C. B. Raleigh, C. H. Scholz, Frictional behavior and constitutive modeling of simulated fault gouge. *J. Geophys. Res.* **95**, 7007–7025 (1990).
18. P. L. Moore, N. R. Iverson, Slow episodic shear of granular materials regulated by dilatant strengthening. *Geology* **30**, 843–846 (2002).
19. P. Segall, J. R. Rice, Dilatancy, compaction, and slip instability of a fluid-infiltrated fault. *J. Geophys. Res.* **100**, 22155–22171 (1995).
20. Y. Liu, A. M. Rubin, Role of fault gouge dilatancy on aseismic deformation transients. *J. Geophys. Res.* **115**, B10414 (2010).
21. P. Segall, A. M. Rubin, M. Bradley, J. R. Rice, Dilatant strengthening as a mechanism for slow slip events. *J. Geophys. Res.* **115**, B12305 (2010).
22. Y. J. Liu, J. J. McGuire, M. D. Behn, Frictional behavior of oceanic transform faults and its influence on earthquake characteristics. *J. Geophys. Res.* **117**, B04315 (2012).
23. J. H. Dieterich, Modeling of rock friction 1. Experimental results and constitutive equations. *J. Geophys. Res.* **84**, 2161–2168 (1979).
24. A. L. Ruina, Slip instability and state variable friction laws. *J. Geophys. Res.* **88**, 10359–10370 (1983).
25. C. He, Z. Wang, W. Yao, Frictional sliding of gabbro gouge under hydrothermal conditions. *Tectonophys.* **445**, 353–362 (2007).
26. Y. Kaneko, J. Avouac, N. Lapusta, Towards inferring earthquake patterns from geodetic observations of interseismic coupling. *Nat. Geosci.* **3**, 363–369 (2010).
27. W. H. Bakun *et al.*, Implications for prediction and hazard assessment from the 2004 Parkfield earthquake. *Nature* **437**, 969–974 (2005).
28. A. M. Rubin, D. Gillard, J. L. Got, Streaks of microearthquakes along creeping faults. *Nature* **400**, 635–641 (1999).
29. J. Jiang, Y. Fialko, Reconciling seismicity and geodetic locking depths on the Anza section of the San Jacinto Fault. *Geophys. Res. Lett.* **43**, 10,663–10,671 (2016).
30. J. Samuelson, D. Elsworth, C. Marone, Shear-induced dilatancy of fluid saturated faults: Experiment and theory. *J. Geophys. Res.* **114**, B12404 (2009).
31. J. Samuelson, D. Elsworth, C. Marone, Influence of dilatancy on the frictional constitutive behavior of a saturated fault zone under a variety of drainage conditions. *J. Geophys. Res.* **116**, B10406 (2011).

32. R. Lohman, J. McGuire, Earthquake swarms driven by aseismic creep in the Salton Trough, California. *J. Geophys. Res.* **112**, 1–10 (2007).
33. H. Hirose, T. Matsuzawa, T. Kimura, H. Kimura, The Boso slow slip events in 2007 and 2011 as a driving process for the accompanying earthquake swarm. *Geophys. Res. Lett.* **41**, 2778–2785 (2014).
34. H. Dragert, K. Wang, T. S. James, A silent slip event on the deeper Cascadia subduction interface. *Science* **292**, 1525–1528 (2001).
35. K. Obara, H. Hirose, F. Yamamizu, K. Kasahara, Episodic slow slip events accompanied by non-volcanic tremors in southwest Japan subduction zone. *Geophys. Res. Lett.* **31**, L23602 (2004).
36. L. A. Reinen, J. D. Weeks, T. E. Tullis, The frictional behavior of lizardite and antigorite serpentinites - experiments, constitutive models, and implications for natural faults. *Pure. Appl. Geophys.* **143**, 317–358 (1994).
37. E. Roland, J. J. McGuire, Earthquake swarms on transform faults. *Geophys. J. Int.* **178**, 1677–1690 (2009).
38. S. Holtkamp, M. Brudzinski, Megathrust earthquake swarms indicate frictional changes which delimit large earthquake ruptures. *Earth Planet Sci. Lett.* **390**, 234–243 (2014).
39. S. Wei *et al.*, The 2012 Brawley swarm triggered by injection-induced aseismic slip. *Earth Planet Sci. Lett.* **422**, 115–125 (2015).
40. A. Llenos, J. McGuire, Y. Ogata, Modeling seismic swarms triggered by aseismic transients. *Earth Planet Sci. Lett.* **281**, 59–69 (2009).
41. X. Chen, P. Shearer, R. Abercrombie, Spatial migration of earthquakes within seismic clusters in Southern California: Evidence for fluid diffusion. *J. Geophys. Res.* **117**, B04301 (2012).
42. Y. Ito *et al.*, Episodic slow slip events in the Japan subduction zone before the 2011 Tohoku-Oki earthquake. *Tectonophys.* **600**, 14–26 (2013).
43. E. Brodsky, T. Lay, Recognizing foreshocks from the 1 April 2014 Chile earthquake. *Science* **344**, 700–702 (2014).
44. A. M. Rubin, Episodic slow slip events and rate-and-state friction. *J. Geophys. Res.* **113**, B11414 (2008).
45. J. R. Rice, Spatiotemporal complexity of slip on a fault. *J. Geophys. Res.* **98**, 9885–9907 (1993).
46. K. Mizoguchi, T. Hirose, T. Shimamoto, E. Fukuyama, Internal structure and permeability of the Nojima fault, southwest Japan. *J. Struct. Geol.* **30**, 513–524 (2008).